

## Article

# Effect of Ultrasonic Vibration Assistance on Microstructure Evolution and Mechanical Properties in Laser-Welded AZ31B Magnesium Alloy

Yulang Xu, Jingyong Li \*, Yanxin Qiao \*, Weidong Wang, Xuzhi Lan and Xuyang Guo

Advanced Welding Technology Provincial Key Laboratory, Jiangsu University of Science and Technology, Zhenjiang 212003, China; yulang\_xu@163.com (Y.X.); xuzhi\_lan@126.com (X.L.)

\* Correspondence: lijingyong@just.edu.cn (J.L.); yxqiao@just.edu.cn (Y.Q.)

**Abstract:** Given the susceptibility to weld porosity and poor weld formability in laser beam welding (LBW), this study delves into an examination of the impact of ultrasonic vibrations on microstructural morphologies and mechanical properties in AZ31B magnesium (Mg) alloy. A comparative analysis was conducted between ultrasonic vibration-assisted LBW and conventional LBW. The results established that the effective elimination of weld porosity, an outcome attributed to the combined effects of cavitation and acoustic streaming, resulted in a weld characterized by a visually seamless and structurally robust appearance. Furthermore, the incorporation of ultrasonic vibration assistance in the welding process yielded a finer microstructure as compared to the conventional LBW. Moreover, the lamellar structures of  $\beta$ -Mg<sub>17</sub>Al<sub>12</sub> were transformed into particles and evenly distributed throughout the  $\alpha$ -Mg matrix. In addition, the incorporation of 50% ultrasonic vibration assistance yielded notable improvements in tensile strength (259.6 MPa) and elongation (11.1%). These values represented enhancements of 4.8% and 35.4% as compared to joints fabricated by using conventional LBW.

**Keywords:** AZ31B; laser beam welding; ultrasonic vibration; microstructure; mechanical properties



**Citation:** Xu, Y.; Li, J.; Qiao, Y.; Wang, W.; Lan, X.; Guo, X. Effect of Ultrasonic Vibration Assistance on Microstructure Evolution and Mechanical Properties in Laser-Welded AZ31B Magnesium Alloy. *Metals* **2024**, *14*, 35. <https://doi.org/10.3390/met14010035>

Academic Editor: Soran Biroscu

Received: 23 November 2023

Revised: 22 December 2023

Accepted: 26 December 2023

Published: 28 December 2023



**Copyright:** © 2023 by the authors. Licensee MDPI, Basel, Switzerland. This article is an open access article distributed under the terms and conditions of the Creative Commons Attribution (CC BY) license (<https://creativecommons.org/licenses/by/4.0/>).

## 1. Introduction

Due to their status as the most lightweight structural metals, magnesium (Mg) alloys are extensively applied in various industries, including transportation and aerospace. This preference is primarily attributed to their low density and remarkable specific strength [1–3]. In contrast to traditional steel and aluminium (Al) materials [4,5], the integration of Mg alloys in the construction of typical automobile parts leads to a notable decline in overall weight. Such a decline is in line with the broader objectives of fostering energy conservation and reducing emissions in the automotive sector [6,7]. Moreover, Mg alloys are well-suited for deployment in digital products as replacements for engineering plastics and Al alloys due to their lightweight and adaptable characteristics [8]. In addition, Mg alloys have emerged as a favorable material option for surgical implants due to the fact that their elastic modulus closely resembles that of the human skeleton [9].

In order to expand the range of potential applications for Mg alloys, it becomes imperative to delve into the realms of welding and joining. Numerous techniques have been developed for welding and joining Mg alloys, including but not limited to methods such as friction stir welding (FSW) [10], tungsten-inert gas welding [11], electron beam welding [12] and laser beam welding, etc. [13–15]. To enhance the overall mechanical properties performance of welded joints, it is a common practice to administer post-welding treatments, including heat treatment [16] and cryogenic treatment [17]. Simultaneously, the welding process is bolstered by the integration of external field assistance [18,19], with ultrasonic vibration assistance being a notable example. Based on straightforward yet efficient physical principles intended to enhance grain refinement and eradicate weld pores throughout the solidification process, a specialized apparatus was engineered which

enabled the application of high-frequency vibrations to the workpiece during welding. This method has emerged as a prominent and actively researched avenue in the field of Mg alloy welding.

Yang [20] conducted a welding experiment involving 2-mm-thick dissimilar Mg alloys MB3 and AZ31 using the GTAW method. Notably, the introduction of ultrasonic vibration assistance effectively mitigated nearly all porosity defects in the weld. Additionally, the coarse  $\alpha$ -Mg grains in the fusion zone were refined to a size of 26  $\mu\text{m}$ , and the refinement and uniform distribution of  $\text{Mg}_{17}\text{Al}_{12}$  precipitation phases were attributed to the effects induced by cavitation and acoustic streaming. The application of an optimal ultrasonic power level, precisely set at 1.0 kW, resulted in a substantial elevation in the microhardness within the fusion zone of the AZ31/MB3 joint, achieving a value of 53.5 HV. This concurrent enhancement extended to the maximum tensile strength of the joints, reaching 263 MPa and ultimately leading to fracture initiation within the AZ31 Mg alloy base plate. Xu et al. [21] pioneered the development of a cutting-edge technology that integrated ultrasonic assistance into the tungsten inert-gas welding-brazing process. Their investigation revealed that, when employing an ultrasonic power of 1.2 kW, a transformative effect can be observed in the morphology of columnar  $\alpha$ -Mg grains, which results in a transition to approximately equiaxed grains. This transformation was accompanied by a noteworthy reduction in the average grain size of columnar grains from 200  $\mu\text{m}$  to 50  $\mu\text{m}$ . Furthermore, the joints displayed an exceptional strength of 239 MPa, representing 93% of the strength observed in the parent Mg alloy. Notably, the fracture surface displayed distinctive attributes indicative of a plastic fracture. In the research conducted by Lei et al. [22], an in-depth analysis was carried out on a 3-mm-thick AZ31B Mg alloy welded using LBW in conjunction with ultrasonic vibration assistance. Their investigation revealed a substantial reduction in weld porosity from 359.9  $\mu\text{m}^2$  to 213.7  $\mu\text{m}^2$ . Furthermore, there was a noteworthy reduction of 41.6% in the average grain area relative to its state in the as-welded condition. Moreover, the process of effective grain refinement and pore elimination led to a notable enhancement in both tensile strength and elongation, resulting in values of 274.1 MPa and 7.5%, respectively. These results represent a remarkable increase of 16.6% and 13.6% over the as-welded joint. Baradaran et al. [23] achieved the successful welding of an AZ91C Mg alloy through the utilization of ultrasonic vibration assistance combined with FSW. Their findings indicated substantial improvements in tensile strength and yield strength. Specifically, these properties were enhanced from initial values of 195 MPa, 115 MPa, and 4% to 225 MPa, 130 MPa, and 5%, respectively, due to the grain refinement within the stir zone.

In this present investigation, AZ31B Mg alloy plates were selected as the base metal (BM). The ultrasonic-assisted LBW process was carried out to examine the impact of ultrasonic vibration amplitude on the microstructure evolution and the resulting mechanical properties of the welded joints in the Mg alloy. These explorations are intended to serve as a reliable resource and as foundational data for advancements in the fields of Mg alloy welding and joining.

## 2. Experimental Procedures

### 2.1. Materials and Welding Equipment

The BMs chosen for the ultrasonic vibration-assisted LBW procedure were commercial AZ31B Mg alloy plates measuring 100 mm  $\times$  100 mm  $\times$  4 mm (length  $\times$  width  $\times$  thickness). These plates exhibited a microstructure characterized by fine equiaxed grains, with an average grain size of 16  $\mu\text{m}$ , as visually depicted in Figure 1. The BM comprised a composite structure of  $\alpha$ -Mg and  $\beta$ -phase components. In the  $\alpha$ -Mg matrix, a minor proportion of the  $\beta$ -phase was evenly dispersed. Notably, the  $\beta$ -phase, identified through X-ray diffraction (XRD) analysis, was confirmed as  $\text{Mg}_{17}\text{Al}_{12}$ , as depicted in Figure 1. Through energy spectrum analysis, the chemical composition of the BM was elucidated, revealing a composition comprising Al 3.18 wt.%, Zn 1.26 wt.%, Mn 0.36 wt.%, Si 0.02 wt.%, and Mg Bal. Prior to the welding process, surface preparations were undertaken on the BM. These preparations involved the removal of oxide layers and greasy contaminants through

abrasion with emery paper. Subsequently, the surfaces were cleansed with absolute ethanol and maintained in a dry environment in readiness for welding.

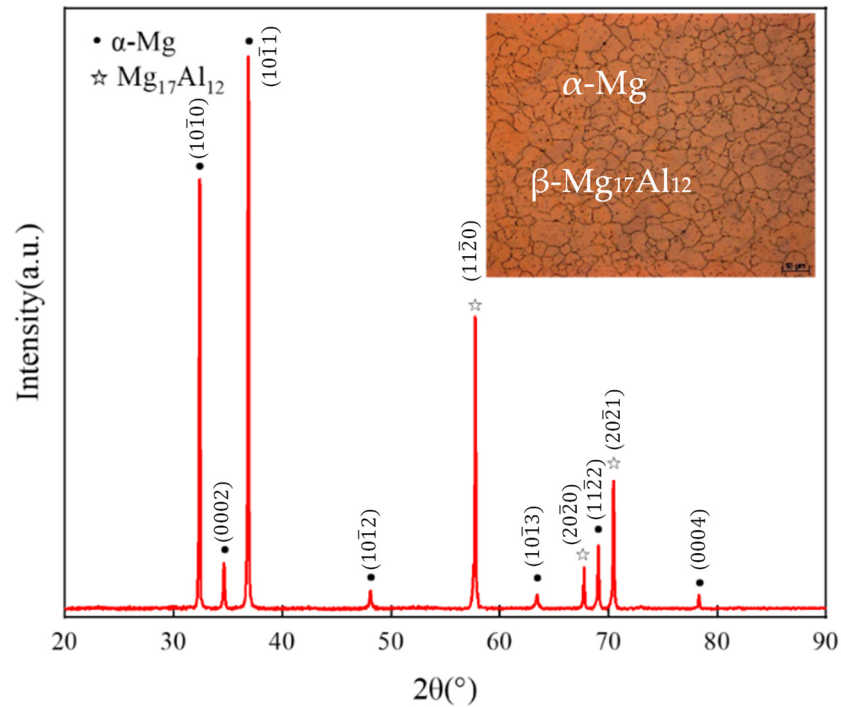


**Figure 1.** Microstructure of the AZ31B base metal.

The laser beam welder and ultrasonic vibration equipment are shown in Figure 2a,b, respectively. The LBW was performed using a fiber laser system with a rated power of 6.0 kW (IPG YLS-6000-S2-TR). The ultrasonic vibration-assisted equipment included a 20 kHz fixed-frequency ultrasonic generator (YPJ13-U055) with a maximum output of 1.5 kW. Additionally, the setup incorporated a piezoelectric ceramic vibration transducer, a specially designed tapered horn resonator, and a supporting frame. The maximum amplitude deviation of the ultrasonic tool head was recorded at 16  $\mu\text{m}$ . In this experimental context, a selection of five different amplitude settings was chosen, with Table 1 presenting the relationship between vibration amplitude and the resulting vibration offsets.

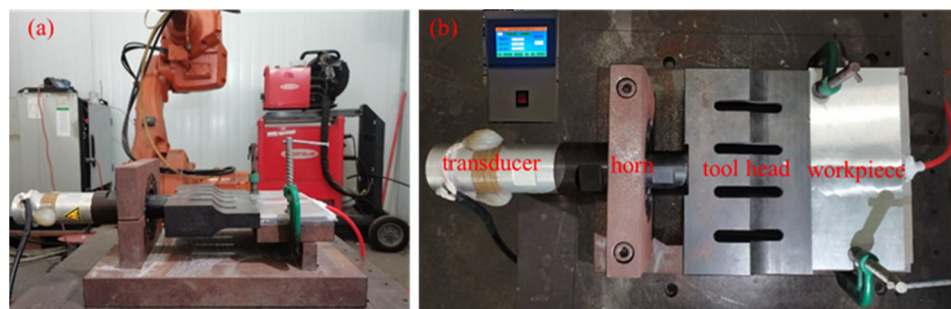


**Figure 2.** The equipment of ultrasonic vibration-assisted laser welding. (a) laser welder (b) ultrasonic vibration equipment.

**Table 1.** Relationship between the vibration amplitude and the vibration offsets.

| Proportion of max vibration amplitude | 10% | 30% | 50% | 70% | 90%  |
|---------------------------------------|-----|-----|-----|-----|------|
| Vibration offset ( $\mu\text{m}$ )    | 0   | 1.6 | 4.8 | 8   | 14.4 |

## 2.2. Testing Equipment

A comprehensive array of investigative techniques was used to unravel the intricate mechanisms underpinning the influence of ultrasonic treatment upon laser-welded joints in an AZ31 Mg alloy. These techniques encompassed optical microscopy (SZ61 and BX51M; Olympus Co., Ltd., Hamburg, Germany), XRD (SmartLab9kW; Rigaku Co., Ltd., Tokyo, Japan), EDS, and EBSD (S3400N; Hitachi Co., Ltd., Tokyo, Japan). Concurrently, mechanical assessments were carried out, including Vickers hardness (KB30S, KB) and tensile properties (CMT5205, MTS).

## 3. Results and Discussion

### 3.1. Macrostructural Analysis

To prevent the oxidation of the molten pool, a shielding gas comprising high-purity argon with a purity level of 99.99% was coaxially delivered at a flow rate of 20 L/min. The LBW process was meticulously configured with specific parameters: an output power ( $P$ ) set at 2 kW, a welding speed ( $v$ ) established at 30 mm/s, and an absence of defocusing ( $\Delta f = 0$  mm). Under the influence of these specific welding technological parameters, the macroscopic features of the AZ31B Mg alloy laser-beam-welded joint, including the frontal and rear bead appearances as well as the cross-sectional view, are vividly illustrated in Figure 3a. Clearly observable is the persistence of a collapse defect when a high welding speed is employed, coupled with a noticeable coarseness in the texture of the fillet on the weld surface.

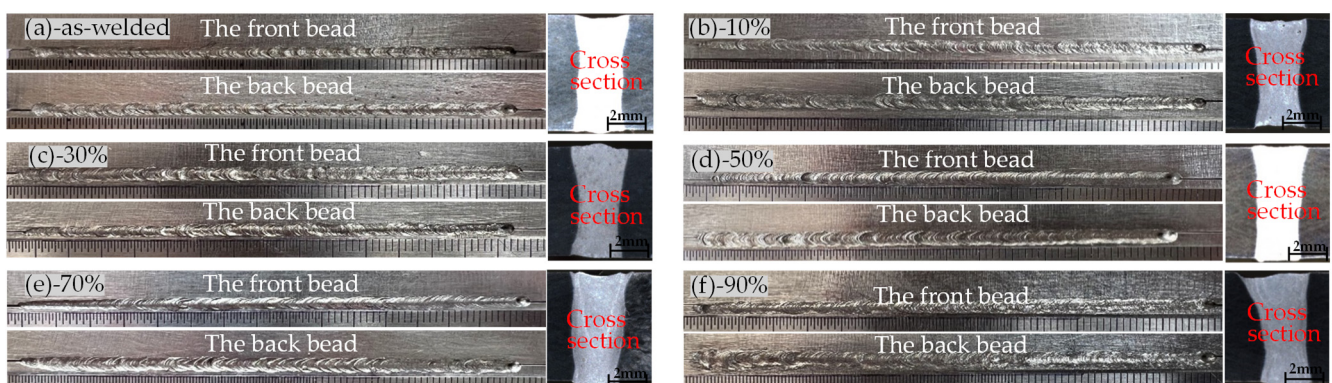


**Figure 3.** The weld appearance of the welded joints with and without ultrasonic vibration.

Following the introduction of ultrasonic vibration, particularly at a 50% vibration amplitude, a notable amelioration was evident in the susceptibility of the welding joint to collapse. Furthermore, the visual representation of the weld bead surpassed that of the initial, as-welded joint, as characterized by a notably smoother and more robust configuration which is illustrated in Figure 3d. Interestingly, an excessive utilization of ultrasonic power yielded limited improvements in microstructure refinement. Conversely, it tended to engender welding defects within the weld zone (WZ) and subsequently diminished the mechanical properties of the material.

### 3.2. Microstructure Evolution Analysis

#### 3.2.1. Metallographic Analysis

Figure 4 provides a visual representation of the characteristic microstructure in the proximity of the fusion boundary within the welded joint, showcasing the disparities between the joints fabricated with and without the application of ultrasonic vibration assistance. As elucidated in Figure 4a, when progressing from left to right, the welded joints could be categorized into four distinct regions: the BM, the heat-affected zone (HAZ), the fusion line (FL), and the weld center (WC). As a result of the thermal cycle induced by welding, a slight augmentation was noted in the grain sizes in the HAZ relative to those found in the BM. In line with this observation, Min et al. [24] conducted

a comprehensive investigation into the TIG welding process as applied to the AZ61 Mg alloy. Their findings substantiated the fact that the grain size within this region undergoes enlargement when the welding temperature within this zone exceeds its recrystallization threshold. Conversely, the propensity for grain growth within the HAZ of the laser-welded joint was less pronounced due to the heightened precision and diminished spot diameter, in contrast to the conventional fusion-welding techniques. In addition, a substantial quantity of dark precipitated particles was generated and evenly dispersed in the grains and along the grain boundaries. This observation unraveled a distinct blurring of the grain boundary, which could be attributed to the precipitation of a noticeable quantity of segregations caused by non-equilibrium solidification. This particular phenomenon arose due to the considerable heat input during the welding procedure, followed by rapid cooling subsequent to welding. Interestingly, prior experimental findings have corroborated this observation, suggesting that the black precipitated particles were manifestations of segregated superionic metal atoms [11].

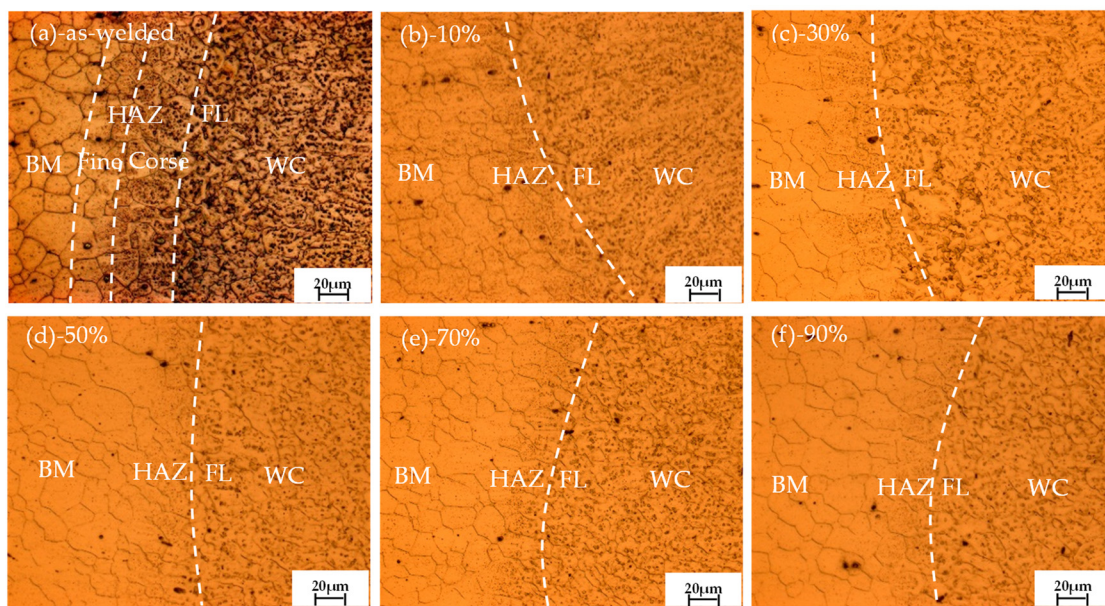


**Figure 4.** Microstructure observation of the welded joint with different vibration amplitudes.

As presented in Figure 4b–f, the application of ultrasonic vibration resulted in a notable augmentation of heterogeneous nucleating particles within the weld pool. This observation signifies the attainment of effective grain refinement facilitated by the application of ultrasonic processing. Moreover, Ramirez et al. [25] asserted that the collapse of bubbles occurs due to the cavitation effect, during which the impact wave generated in this process fractures the newly formed dendrite structures. Consequently, these fragmented dendrites can serve as fresh nucleation particles. Additionally, the introduction of ultrasonic vibration to the welding process leads to a reduction in undercooling. These combined effects contribute positively to the formation of equiaxed grains. The research of Xu et al. [26] delved into the interplay between the energy barrier associated with heterogeneous nucleation and the phenomenon of undercooling. Their findings substantiated the fact that a reduction in undercooling facilitates grain nucleation, resulting in an increased formation of equiaxed grains under uniform temperature gradients. Simultaneously, the thermal effect leads to a decrease in the solidification rate of the weld pool, thereby aiding the expulsion of bubbles. Nevertheless, the prolongation of solidification time amplifies the propensity for grain size enlargement, which is counterproductive to grain refinement. Conversely, in the context of ultrasonic vibration-assisted LBW, the heightened presence of nucleation particles assumes a predominant role, leading to a marked enhancement in the grain refinement process.

### 3.2.2. Phase Analysis

In terms of XRD analyses, the weld seam subjected to ultrasonic vibration and the one without ultrasonic vibration, under otherwise identical conditions, were examined. As shown in Figure 5, the phase composition in the weld seam remained unaltered, consisting solely of  $\alpha$ -Mg and  $\beta$ -Mg<sub>17</sub>Al<sub>12</sub> [27]. It is also noteworthy that the diffraction peak intensity of the  $\beta$ -Mg<sub>17</sub>Al<sub>12</sub> phase remained largely unaffected by this phenomenon. This limited influence could be attributed to the fact that the secondary phase primarily consisted of a small quantity of eutectic  $\beta$ -Mg<sub>17</sub>Al<sub>12</sub>, which posed challenges for detection through the scanning methods. As depicted in Figure 4, the application of ultrasonic vibration assistance induced pronounced lattice distortion, resulting in an increase in the axial ratio from 1.62270 to 1.62580 and a corresponding reduction in lattice symmetry.

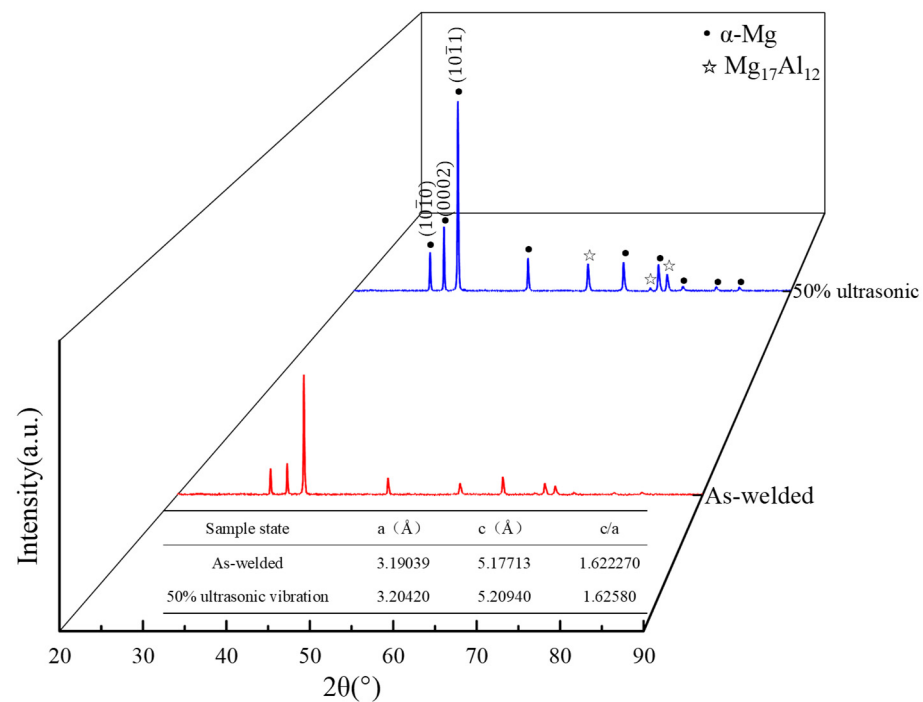


**Figure 5.** XRD patterns of the weld seam with and without ultrasonic vibration assistance.

Figure 6 presents the scanning electron microscope (SEM) images depicting the morphological characteristics near the fusion line of both the as-welded and ultrasonic vibration-assisted welded joints. As observed in Figure 6a,c, there was a consistent absence of notable variations in the elemental content from the BM to the WC, with only marginal fluctuations observed. Furthermore, the analysis of the  $\alpha$ -Mg matrix and the secondary phase using EDS revealed their predominant composition to be Mg and Al. Notably, the Al content within the  $\alpha$ -Mg matrix slightly surpassed that of the raw BM. This disparity could be attributed to the LBW process causing some Mg element loss, consequently leading to an elevated proportion of Al element content. As shown in Figure 6b, the secondary phases were predominantly distributed inside the grain structure, which aligns with the observations in Figure 4. When a 50% amplitude ultrasonic vibration was applied, the  $\beta$ -Mg<sub>17</sub>Al<sub>12</sub> phases underwent a transformation from coarseness into particulate form and were dispersed within the  $\alpha$ -Mg matrix. This transformation was a result of the cavitation and acoustic streaming triggered by the ultrasonic vibration, as illustrated in Figure 6d.

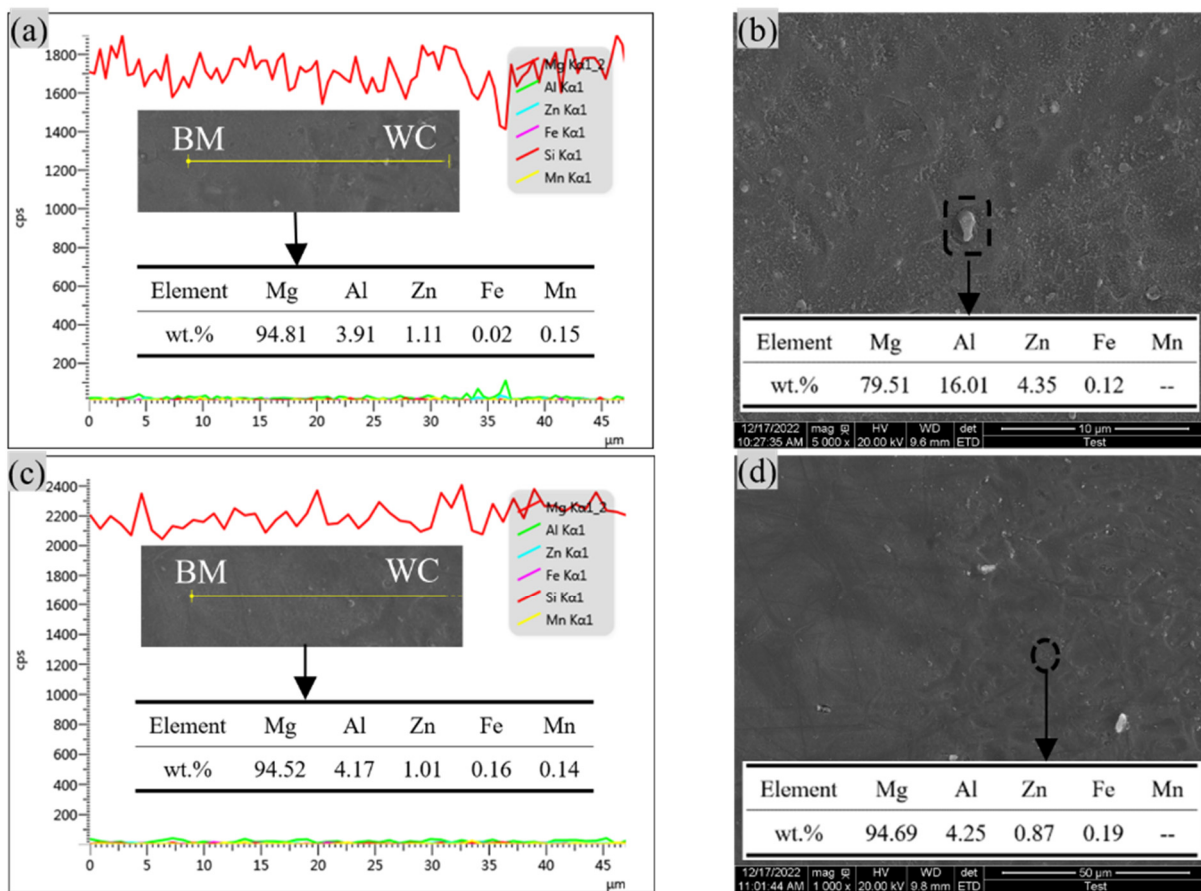


**Figure 6.** Results of the SEM in the welded joint with and without ultrasonic vibration assistance. (a) element distribution of the weld seam without ultrasonic assistance (b) EDS of second phase in weld seam without ultrasonic assistance. (c) element distribution of the weld seam with ultrasonic assistance (d) EDS of second phase in weld seam with ultrasonic assistance.

### 3.2.3. EBSD Analysis

A calibration process was performed for each region within the laser-welded joint, and Figure 7 presents the grain orientation map in the vicinity of the FL of the welded joint. The orientation distribution map visually unravels the distinctions in the size and morphology of the WZ, the HAZ, and the BM in the cross-sectional area of the welded joint. In the cross-section of the welded joint, notable differences in grain size are evident: the weld seam exhibits the smallest grain size, the HAZ displays the largest grain size, and the BM falls in-between. This discrepancy can be attributed to the relatively rapid cooling rate experienced by the WZ, which causes the grains to preferentially grow along the direction with the most pronounced temperature gradient [28,29].

Furthermore, the grain orientation distribution in the three regions can be deduced by examining the grain orientation distribution map. Distinct colors differentiate the grains with varying orientations, and the regions exhibiting analogous orientation color patterns share similar characteristics. It is important to note that the BM area, being a hot-rolled Mg alloy, maintains a certain level of preferred orientation following processing, resulting in relatively subtle distinctions in color distribution. The primary distinction can be observed in the red section, where the HAZ appeared relatively narrow, and its grain size experienced a minor increase as compared to the BM zone. Moreover, little difference was noted in grain orientation relative to the BM. Conversely, the grains within the WZ exhibited substantial refinement, featuring pronounced differences in color distribution. This discrepancy suggests a random grain orientation distribution within the WZ, which is characterized by an absence of specific orientation and a notably low texture strength,

with almost no evident texture. In the pole diagram, it is evident that the maximum pole density of the texture declined from 8.94 to 6.54 when 50% ultrasonic vibration assistance was applied, in comparison to the as-welded joint.

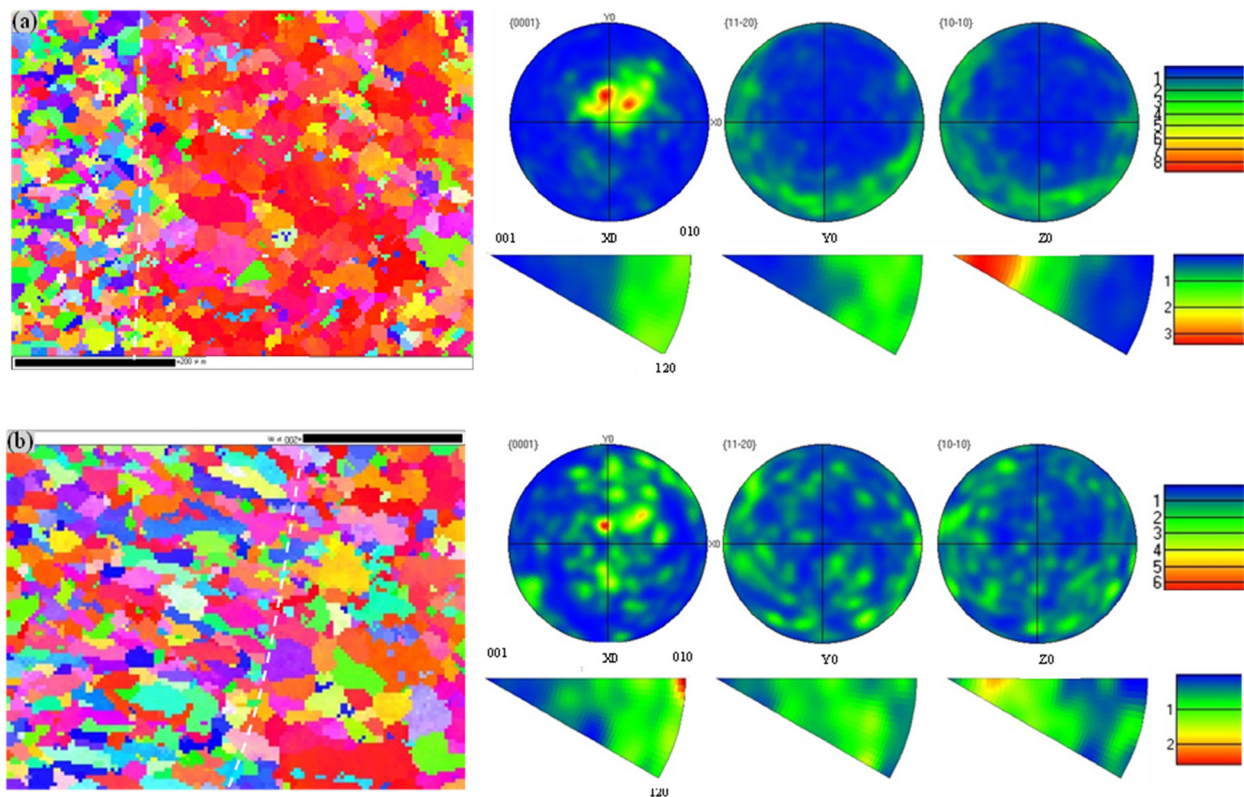


**Figure 7.** IPF, pore figure, and inverse pole figure map of the weld seam with and without ultrasonic vibration assistance. (a) EBSD testing result of weld seam in the as-welded joint (b) EBSD testing result of weld seam in the joint with 50% ultrasonic assistance.

### 3.3. Mechanical Property Analysis

#### 3.3.1. Microhardness Analysis

Due to the similarity of the microhardness test results under different ultrasonic amplitudes and in order to better demonstrate the effects of ultrasonic assistance on the microhardness of welded joints, 0%, 50%, and 90% vibration amplitudes were selected. Figure 8 illustrates a comparison of the microhardness profiles for the Mg alloy joints obtained with 50% and 90% amplitude and without the assistance of ultrasonic vibration. Microhardness measurements were conducted along the horizontal direction of the joint. Progressing in a gradual manner from the BM of the Mg alloy toward the WC, a noteworthy observation becomes apparent: for the as-welded sample, the microhardness in HAZ was not notably lower than that within the WZ, which could potentially be attributed to the presence of  $Mg_{17}Al_{12}$  in this specific region. It is worth noting that due to the relatively larger grain size present in the BM in comparison to that present within the WC, the microhardness value within the BM was the lowest.

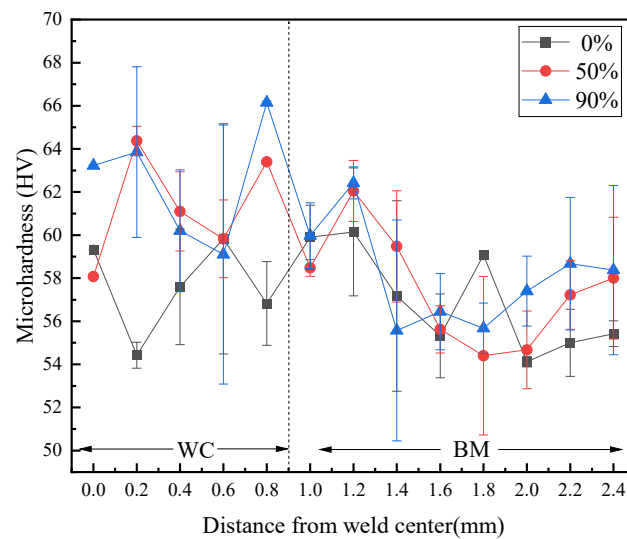


**Figure 8.** Microhardness distribution of the welded joints with and without ultrasonic vibration assistance.

Upon the application of ultrasonic vibration, a noticeable enhancement was observed in the microhardness of the WC, surpassing the levels attained without ultrasonic assistance, as shown in Figure 8. Furthermore, as the ultrasonic amplitude was progressively elevated, a consistent and continuous augmentation was noted in the microhardness of the WZ. The examination revealed that, in the case of a 50% vibration amplitude, the microhardness levels displayed decline in variations due to the successful refinement and evenness achieved in the microstructure. Conversely, when the vibration amplitude was elevated to 90%, it led to higher microhardness values accompanied by more pronounced fluctuations [21]. This phenomenon can be attributed to the excessive vibration amplitude, which can induce voids and, in some cases, cause cracks within the weld, consequently diminishing the quality of the welding.

### 3.3.2. Tensile Properties Analysis

As illustrated in Figure 9a, the tensile strength of the Mg alloy joints subjected to ultrasonic enhancement exhibited a notable improvement as compared to joints welded without the assistance of ultrasonic vibration. These experimental results align with the Hall-Petch relationship, indicating that the enhanced strength is primarily attributed to the refinement of the grain structure. The application of a 50% increase in ultrasonic vibration amplitude resulted in a notable enhancement in the ultimate tensile strength, showing a 4.8% increase from 247.7 MPa to 259.6 MPa. Furthermore, the elongation exhibited a substantial augmentation of 35.4%, rising from 8.2% to 11.1%. Nevertheless, when the ultrasonic vibration amplitude was further raised to 90%, both the tensile strength and elongation underwent a decline, decreasing from 259.6 MPa and 8.2% to 243.9 MPa and 6.0%, respectively. This decline can be attributed to the unstable solidification process under the conditions of excessive vibration amplitude. In addition, except for 50% amplitude ultrasonic vibration-assisted samples, which fractured near the fusion line, samples of as-welded and other ultrasonic vibration-assisted amplitudes all fractured at the center of the weld seam.

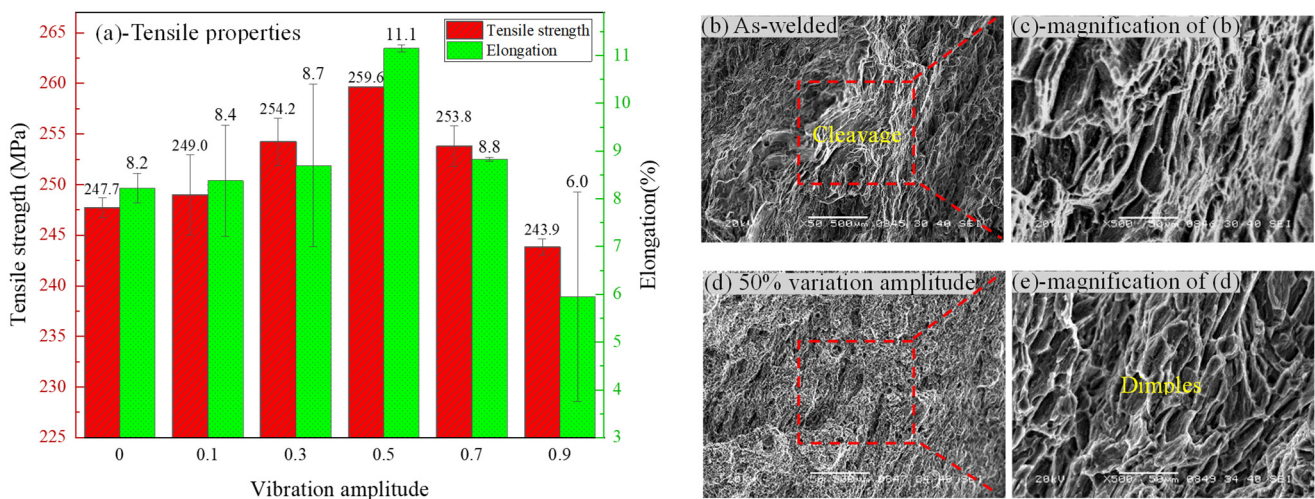


**Figure 9.** Tensile properties and fracture morphologies of the welded joints with and without ultrasonic vibration assistance. (a) tensile properties (b) low magnification fracture morphologies of as-welded joint (c) high magnification fracture morphologies of as-welded joint (d) low magnification fracture morphologies with 50% ultrasonic assistance (e) high magnification fracture morphologies with 50% ultrasonic assistance.

Figure 9b–e presents the fracture characteristics of the tensile specimens, both with and without the assistance of ultrasonic vibration, in the form of welded joints. Figure 9b,c exhibits the presence of considerable quasi-cleavage splinter layers, indicating a brittle fracture behavior, alongside a few dimples that signify ductile fracture behavior. The predominant fracture mode observed in the LBW-welded joints is a combination of brittleness and ductility, with a dominant brittle component. This behavior can be attributed to the composition of the AZ31B alloy, which primarily comprises the  $\alpha$ -Mg matrix with inherent plasticity and the brittle  $\beta$ -Mg<sub>17</sub>Al<sub>12</sub> phase. Furthermore, the non-equilibrium solidification process during LBW contributes to the increased presence of the brittle  $\beta$ -phase. Consequently, stress concentration tends to occur more readily in this region. However, the implementation of ultrasonic vibration assistance leads to a substantial reduction in the number of welding pores. This observation is consistent with findings reported in a prior study [30]. Alavi et al. [30] demonstrated that the ultrasonic vibration-induced enhancement of melt flow results in a reduction of porosity defects within the welded joint. This reduction is accompanied by a decrease in cleavage steps in the fracture area and a slight increase in the number of dimples, signifying an improvement in the plasticity of the ultrasonic vibration-assisted joint.

#### 4. Conclusions

(1) Ultrasonic vibration-assisted welding can enhance grain refinement and promote uniformity in microstructures, but this effect is only observed within a specific range of vibration amplitudes. If the vibration amplitude is raised to 90%, it results in a decline in the overall macroscopic quality of the welded joints and a significant decrease in the tensile properties of the material.

(2) In the pole diagram, the maximum pole density of the texture is reduced from 8.94 to 6.54 when utilizing 50% ultrasonic vibration assistance in comparison to the as-welded joint.

(3) The microhardness of the WZ displays more stability and reduced fluctuations when subjected to 50% vibration amplitude due to the effective refinement and homogenization of the microstructure facilitated by ultrasonic vibration. Conversely, when the vibration amplitude is elevated to 90%, it results in higher microhardness values and is accompanied by more pronounced fluctuations.

(4) The sample subjected to a 50% vibration amplitude displays notable improvements in tensile strength (259.6 MPa) and elongation (11.3%), demonstrating increases of 4.8% and 35.4%, respectively, as compared to the as-welded joint. Additionally, the fracture morphology displays characteristics consistent with quasi-cleavage fractures.

**Author Contributions:** Conceptualization: Y.X., J.L. and Y.Q.; Methodology: Y.X., J.L. and Y.Q.; Software: Y.X., W.W., X.L., X.G. and Y.Q.; Validation: W.W., X.L. and Y.Q.; Formal Analysis: Y.X., W.W., X.L., X.G. and Y.Q.; Investigation: Y.X., W.W., X.L. and Y.Q.; Resources: Y.X., J.L. and Y.Q.; Data Curation: W.W., X.L. and Y.Q.; Writing—Original Draft Preparation: Y.X.; Writing—Review & Editing: J.L. and Y.Q. All authors have read and agreed to the published version of the manuscript.

**Funding:** This work is funded by the Science Foundation of Jiangsu Province (BK20180984) and the National Natural Science Foundation of China (Grant Nos. 52005228, 51975263).

**Institutional Review Board Statement:** Not applicable.

**Informed Consent Statement:** Not applicable.

**Data Availability Statement:** The data used to support the findings of this study are available from the corresponding author upon request. The data are not publicly available due to privacy.

**Conflicts of Interest:** The authors declare no conflicts of interest.

## References

1. Song, J.; She, J.; Chen, D.; Pan, F. Latest research advances on magnesium and magnesium alloys worldwide. *J. Magnes. Alloys* **2020**, *8*, 1–41. [[CrossRef](#)]
2. Yang, Y.; Xiong, X.; Chen, J.; Peng, X.; Chen, D.; Pan, F. Research advances in magnesium and magnesium alloys worldwide in 2020. *J. Magnes. Alloys* **2021**, *9*, 705–747. [[CrossRef](#)]
3. Song, J.; Chen, J.; Xiong, X.; Peng, X.; Chen, D.; Pan, F. Research advances of magnesium and magnesium alloys worldwide in 2021. *J. Magnes. Alloys* **2022**, *10*, 863–898. [[CrossRef](#)]
4. Qiao, Y.X.; Zheng, Z.B.; Yang, H.K.; Long, J.; Han, P.X. Recent progress in microstructural evolution, mechanical and corrosion properties of medium-Mn steel. *J. Iron Steel Res. Int.* **2023**, *30*, 1463–1476. [[CrossRef](#)]
5. Sheng, S.L.; Qiao, Y.X.; Zhai, R.Z.; Sun, M.Y.; Xu, B. Processing map and dynamic recrystallization behaviours of 316LN-Mn austenitic stainless steel. *Int. J. Miner. Metall. Mater.* **2023**, *30*, 2386–2396. [[CrossRef](#)]
6. Tan, J.; Ramakrishna, S. Applications of Magnesium and Its Alloys: A Review. *Appl. Sci.* **2021**, *11*, 6861. [[CrossRef](#)]
7. Seetharaman, S.; Jayalakshmi, S.; Arvind Singh, R.; Gupta, M. The Potential of Magnesium-Based Materials for Engineering and Biomedical Applications. *J. Indian Inst. Sci.* **2022**, *102*, 421–437. [[CrossRef](#)]
8. Prasad, S.V.S.; Prasad, S.B.; Verma, K.; Mishra, R.K.; Kumar, V.; Singh, S. The role and significance of Magnesium in modern day research-A review. *J. Magnes. Alloys* **2022**, *10*, 1–61. [[CrossRef](#)]
9. Ramalingam, V.V.; Ramasamy, P.; Kovukkal, M.D.; Myilsamy, G. Research and development in magnesium alloys for industrial and biomedical applications: A review. *Met. Mater. Int.* **2019**, *26*, 409–430. [[CrossRef](#)]
10. Zhao, J.; Wu, C.; Shi, L. Effect of ultrasonic field on microstructure evolution in friction stir welding of dissimilar Al/Mg alloys. *J. Mater. Res. Technol.* **2022**, *17*, 1–21. [[CrossRef](#)]
11. Subravel, V.; Padmanaban, G.; Balasubramanian, V. Effect of welding speed on microstructural characteristics and tensile properties of GTA welded AZ31B magnesium alloy. *Trans. Nonferrous Met. Soc. China* **2014**, *24*, 2776–2784. [[CrossRef](#)]
12. Chen, J.Q.; Li, F.; Wu, Z.G.; Lyu, W.G. Effect of heat input on the microstructure and mechanical properties of an electron-beam-welded AZ31 magnesium alloy. *Mater. Tehnol.* **2020**, *54*, 819–828. [[CrossRef](#)]
13. Xu, Y.L.; Qian, P.; Qiao, Y.X.; Li, J.Y.; Zhang, J.S. Study on laser welding process, microstructure and properties of AZ31B magnesium alloy. *Trans. Indian Inst. Met.* **2022**, *75*, 2905–2912. [[CrossRef](#)]
14. Yang, F.; Liu, B. The effects of ultrasonic vibration on microstructural changes and mechanical properties of Mg alloy joint. *Mater. Res. Express* **2021**, *8*, 026512. [[CrossRef](#)]
15. Min, D.; Shen, J.; Lai, S.; Chen, J.; Xu, N.; Liu, H. Effects of heat input on the low power Nd:YAG pulse laser conduction weldability of magnesium alloy AZ61. *Opt. Lasers Eng.* **2011**, *49*, 89–96. [[CrossRef](#)]
16. Xu, Y.L.; Qian, P.; Li, J.Y.; Qiao, Y.X.; Zhang, J.S.; Liu, J. Effect of solution and aging treatment on microstructure and properties of AZ31B magnesium alloy laser welded joint. *Phys. Met. Metallogr.* **2023**, *123*, 1491–1498. [[CrossRef](#)]
17. Xu, Y.L.; Qian, P.; Qiao, Y.X.; Yin, W.J.; Jiang, Z.W.; Li, J.Y. The influence of heat and cryogenic treatment on microstructure evolution and mechanical properties of laser-welded AZ31B. *Materials* **2023**, *16*, 4764. [[CrossRef](#)]
18. Li, C.; Zhang, X.; Wang, J. The effect of axial external magnetic field on tungsten inert gas welding of magnesium alloy. *Mater. Res. Express* **2018**, *5*, 046531. [[CrossRef](#)]
19. Yuan, T.; Kou, S.; Luo, Z. Grain refining by ultrasonic stirring of the weld pool. *Acta Mater.* **2016**, *106*, 144–154. [[CrossRef](#)]

20. Yang, F.; Zhou, J.; Ding, R. Ultrasonic vibration assisted tungsten inert gas welding of dissimilar magnesium alloys. *J. Mater. Sci. Technol.* **2018**, *34*, 2240–2245. [[CrossRef](#)]
21. Xu, C.; Yuan, X. Effect of ultrasonic field parameters on interfacial characteristics and mechanical properties of Mg alloy welding joint. *Mater. Lett.* **2022**, *306*, 130962. [[CrossRef](#)]
22. Lei, Z.; Bi, J.; Li, P.; Li, Q.; Chen, Y.; Zhang, D. Melt flow and grain refining in ultrasonic vibration assisted laser welding process of AZ31B magnesium alloy. *Opt. Laser Technol.* **2018**, *108*, 409–417. [[CrossRef](#)]
23. Baradarani, F.; Mostafapour, A.; Shalvandi, M. Effect of ultrasonic assisted friction stir welding on microstructure and mechanical properties of AZ91–C magnesium alloy. *Trans. Nonferrous Met. Soc. China* **2019**, *29*, 2514–2522. [[CrossRef](#)]
24. Min, D.; Shen, J.; Lai, S.; Chen, J. Effect of heat input on the microstructure and mechanical properties of tungsten inert gas arc butt-welded AZ61 magnesium alloy plates. *Mater. Charact.* **2009**, *60*, 1583–1590. [[CrossRef](#)]
25. Ramirez, A.; Qian, M.; Davis, B.; Wilks, T.; StJohn, D.H. Potency of high-intensity ultrasonic treatment for grain refinement of magnesium alloys. *Scr. Mater.* **2008**, *59*, 19–22. [[CrossRef](#)]
26. Xu, C.; Sheng, G.; Cao, X.; Yuan, X. Evolution of Microstructure, Mechanical Properties and Corrosion Resistance of Ultrasonic Assisted Welded-Brazed Mg/Ti Joint. *J. Mater. Sci. Technol.* **2016**, *32*, 1253–1259. [[CrossRef](#)]
27. Lei, Z.; Bi, J.; Li, P.; Guo, T.; Zhao, Y.; Zhang, D. Analysis on welding characteristics of ultrasonic assisted laser welding of AZ31B magnesium alloy. *Opt. Laser Technol.* **2018**, *105*, 15–22. [[CrossRef](#)]
28. Coelho, R.S.; Kostka, A.; Pinto, H.; Riekehr, S.; Koçak, M.; Pyzalla, A.R. Microstructure and mechanical properties of magnesium alloy AZ31B laser beam welds. *Mater. Sci. Eng. A* **2008**, *485*, 20–30. [[CrossRef](#)]
29. Wen, T.; Liu, S.-y.; Chen, S.; Liu, L.-t.; Yang, C. Influence of high frequency vibration on microstructure and mechanical properties of TIG welding joints of AZ31 magnesium alloy. *Trans. Nonferrous Met. Soc. China* **2015**, *25*, 397–404. [[CrossRef](#)]
30. Alavi, S.H.; Harimkar, S.P. Melt expulsion during ultrasonic vibration-assisted laser surface processing of austenitic stainless steel. *Ultrasonics* **2015**, *59*, 21–30. [[CrossRef](#)]

**Disclaimer/Publisher's Note:** The statements, opinions and data contained in all publications are solely those of the individual author(s) and contributor(s) and not of MDPI and/or the editor(s). MDPI and/or the editor(s) disclaim responsibility for any injury to people or property resulting from any ideas, methods, instructions or products referred to in the content.